Comparative Assessment of Target Capture Techniques for Space Debris Removal with CubeSats

Comparative Assessment of Target Capture Techniques for Space Debris Removal with CubeSats

Christopher Clark* and Michael Ricard†
The Charles Stark Draper Laboratory, Inc., Cambridge, MA, United States

Daniel E Hastings‡
Department of Aeronautics and Astronautics, 33-207, Massachusetts Institute of Technology, Cambridge, MA, United States

Rebecca Masterson§
Massachusetts Institute of Technology, Cambridge, MA, United States

The use of CubeSats for space debris removal represents a possible avenue for enabling non-governmental operators to become involved in the maintenance of space. While their small size and inexpensive components reduce barriers to entry for universities and companies, certain technical challenges are magnified by CubeSats' low inertia and power limitations. One such area is target capture, in which an approaching CubeSat must establish a secure contact point with a debris object prior to beginning the detumbling or deorbiting process. This paper discusses nets, harpoons, and robotic arms as three possible strategies for target capture. Each method is examined to identify key regimes of possible feasibility for CubeSat applications. A dynamics model is introduced and utilized to simulate the relative motion of a CubeSat tethered to a debris object, a situation encountered with both harpoon and net capture. Differences in potential operating regimes are highlighted for the three methods, and conclusions are drawn about their possible realms of effectiveness.

I. Nomenclature

Abbreviations

ADCS	Attitude determination and control subsystem
ADR	Active debris removal
CONOPS	Concept of operations
TeRBoDOT	Tethered Rigid Body Dynamics Observation Tool

Subscripts and Superscripts

$\vec{(.)}$	Vector
$(.)\|_t$	Indicates quantity $(.)$ at time t

*Draper Fellow, The Charles Stark Draper Laboratory, Inc., Cambridge, MA, United States
†Laboratory Technical Staff, The Charles Stark Draper Laboratory, Inc., Cambridge, MA, United States
‡Professor, Department of Aeronautics and Astronautics, 33-207, Massachusetts Institute of Technology, Cambridge, MA, United States, Honorary Fellow, AIAA
§Principal Research Scientist, Department of Aeronautics and Astronautics, Massachusetts Institute of Technology, Cambridge, MA, United States

Symbols

A	Area
a	Acceleration
a_1, b_1, c_1, d_1, e_1	Intermediate variables used in derivations
D	Diameter
d	Distance
F	Force
I_{deb}	Debris object inertia matrix
l	Length
m	Mass
$P(.)$	Probability of an event
p	Perimeter
r	Radius
s	Shear strength
T	Thickness
t	Time
U	CubeSat volume unit ($10 \times 10 \times 10\ cm$)
v	Velocity
X	Position
XYZ	Inertial coordinate system
α	Incidence angle
Δt	Time step
ΔV	Velocity change
ρ	Density
σ	Standard deviation
τ	Torque
ϕ	Pitch angle
ψ	Yaw angle
ω	Angular velocity

II. Introduction

Space debris around the Earth is a growing problem. The launch of large numbers of satellites for commercial purposes may make the problem worse if they end up contributing to the debris problem and are not properly removed from orbit when their useful life is over. Even if they do not deliberately cause the creation of orbital debris, if a piece of orbital debris collides with them then new rounds of orbital debris will be created. It is hard to deal with a hypervelocity impact.

In previous work, the concept of using a CubeSat or CubeSats was to remove orbital debris was proposed. CubeSats have the advantage of being relatively inexpensive, almost commodities. They can also be built by a wide range of parties who can do some good by building CubeSats to remove debris. With the assumption that the debris is uncooperative, perhaps tumbling and not under active control, a number of techniques have been proposed for the CubeSat to affect the debris object. The techniques basically divide into tow groups. Those which do not have a physical connection between the debris and the CubeSat and those which do have a physical connection. In the first category would be laser ablation to give a ΔV kick to the debris or immersion in the plume of an ion engine to give rise to enhanced drag on a piece of debris. In the second category would be physical connections such as nets, tethers, harpoons and robotic arms. In this work, the focus is on the physical means of affecting debris.

III. Space Debris Capture

As described in Section II, several techniques have been proposed to facilitate docking between a satellite and an uncooperative debris object. At the current time, only three of these techniques—robotic arms, harpoons, and nets—have been successfully demonstrated on-orbit via operational or proof-of-concept missions. In this work, these three methods are highlighted for in-depth analysis as they relate to CubeSat-based ADR. Major considerations include the types of debris (including dynamic properties) that can be handled by each method, constraining factors on feasibility, and areas of relative advantage among the three methods. Analytic methods are used to identify feasible capture scenarios for all methods; Monte Carlo simulation and a two-body dynamics model also allow estimation of success probabilities for the two tether-based capture methods. Each method is discovered to be feasible for certain families of debris objects defined by size and rotation rate.

IV. Robotic Arms

The first of the three selected capture methods is a robotic arm, used to grip the debris object and stabilize the object and CubeSat relative to one another. In this mission scenario, the CubeSat approaches to within a meter of the debris object, matches the object's motion, and manipulates a robotic gripper to clasp a protrusion such as the lip of an engine nozzle or the cable raceway of a rocket body. Once the grip is established, the arm serves as a rigid attachment point for the remainder of the deorbit mission.

One challenge to the robotic arm's success is the requirement for precise relative positioning and motion synchronization. If the debris object has nonzero angular momentum, the CubeSat's limited thrust and attitude control capabilities may prevent it from matching the object's motion. In a recent study, Hakima and Emami [1] concluded that $1^\circ/s$ per axis is the upper limit on debris object angular velocity for an $8U$ deorbiter CubeSat equipped with an ion thruster, reaction wheels, and magnetorquers. They suggest thrust is the primary limiting factor. Since most of the CubeSat designs explored in this work are similarly thrust-constrained, it is assumed that the debris object must have zero angular velocity for a robotic arm capture to take place.

An analysis is performed to determine the robustness of the arm in case the object starts tumbling after capture. Thruster misalignments, for example, could generate torques that impart angular momentum to a previously stable debris object. Feasibility windows are derived to illustrate the maximum angular velocity the arm can withstand from a torque perspective. It is assumed the attachment grip is sufficiently strong to avoid slippage.

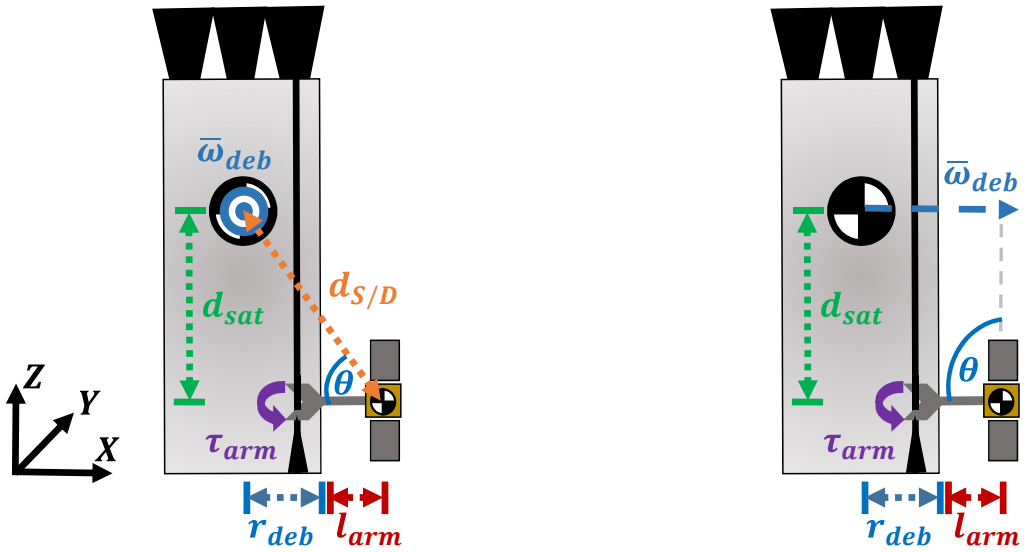

(a) Orientation #1 **(b) Orientation #2**

Fig. 1 Robotic Arm Capture Diagrams

Two cases of a major-axis spin are illustrated in Figure 1. The CubeSat has a mass of m_{sat} and is assumed to be

secured to a raceway or other feature on the debris object's surface. It is located at a distance d_{sat} from the object's center of mass, as measured along the Z-axis. In addition, there is a displacement from the X-axis equal to the object's radius r_{deb} plus the length of the extended robotic arm, l_{arm}, which is assumed to be normal to the object's surface at the point of attachment. The distance between the CubeSat's center of mass and debris object's axis of rotation is marked as $d_{S/D}$. Given this configuration, a minor-axis spin of the object about the Z-axis does not exert torque on the robotic arm, since the direction of the centripetal force is along the arm. A major-axis spin about the X- or Y-axis, on the other hand, generates torque on the arm that depends on the magnitude of the angular velocity vector $\vec{\omega}_{deb}$. In Figure 1a, the angular velocity vector is perpendicular with the robotic arm, while in 1b, it is parallel. Any major-axis spin can be considered a combination of these two cases, since in reality it is unlikely that the arm will remain either parallel or perpendicular with $\vec{\omega}_{deb}$. The equations governing torque on the arm's gripper joint, τ_{arm}, can be readily derived for each of these two cases. In the first case (Figure 1a), the centripetal acceleration of the CubeSat, a_c, can be defined as:

$$a_c = d_{S/D}\omega_{deb}^2 = \sqrt{d_{sat}^2 + (l_{arm} + r_{deb})^2}\,\omega_{deb}^2 \tag{1}$$

Gripper joint torque is then expressed as the norm of the cross product between $\vec{d}_{S/D}$ and centripetal force, $\vec{F}_c$:

$$\tau_{arm} = ||\vec{d}_{S/D} \times \vec{F}_c|| = d_{S/D}F_c sin(\theta) = l_{arm}(m_{sat}d_{S/D}\omega_{deb}^2)(\frac{d_{sat}}{d_{S/D}}) = l_{arm}m_{sat}d_{sat}\omega_{deb}^2 \tag{2}$$

The second case (Figure 1b) is simply a modified version of the first, where $\theta = 90°$ and $d_{S/D} = d_{sat}$. The expression for τ_{arm} reduces to the same quantity derived above. The torque generated on the gripping joint of the robotic arm can now be calculated as a function of the four parameters l_{arm}, m_{sat}, d_{sat}, and ω_{deb} from Equation 2. The parameters of an actual CubeSat robotic arm design are used to estimate l_{arm} and torque capability. REMORA, a proposed debris tracking mission, features a CubeSat-sized robotic arm designed specifically for debris manipulation applications. The arm has a maximum intermittent torque output of 0.75 $N * m$ and a length of 40 cm [2]. These design specifications are used to construct the feasibility envelope of the arm for different CubeSat sizes.

Given the common CubeSat mass limits of 12 kg ($6U$), 16 kg ($8U$), 24 kg ($12U$ and $16U$), and 54 kg ($27U$)*, Figure 2 illustrates the capabilities of the arm for different values of d_{sat} and ω_{deb}. The color scale represents the torque exerted on the arm's gripper joint, and the upper limit of the scale is set equal to the maximum torque capability of the REMORA robotic arm. Any region shaded in color therefore falls within the arm's torque capability. For the 54 kg CubeSat size, the arm is capable of withstanding a major axis spin up to $5°/s$ if the Z-displacement d_{sat} is equal to 5 m. The limit on rotation rate is $7°/s$ for 24 kg, $9°/s$ for 16 kg, and $10°/s$ for 12 kg. These limits are marked with dotted black lines on their respective plots. Note that due to their reduced inertia, any CubeSat sizes smaller than $6U$ generate even less centripetal force and torque for the same position and debris object angular velocity.

If $d_{sat} < 5$ m, the maximum allowable angular velocity increases. A comparison between d_{sat} and maximum allowable angular velocity is presented in Table 1, with accuracy limitations rounded to the nearest tenth.

Table 1 Robotic Arm Required Attachment Accuracy vs. Object Angular Velocity

ω_{deb} (deg/s)	± Accuracy (12 kg)	± Accuracy (16 kg)	± Accuracy (24 kg)	± Accuracy (54 kg)
5	> 5 m	> 5 m	> 5 m	4.7 m
10	> 5 m	3.9 m	2.6 m	1.2 m
15	2.3 m	1.7 m	1.2 m	0.5 m
20	1.3 m	1 m	0.7 m	0.3 m
25	0.8 m	0.6 m	0.4 m	0.2 m

In summary, robotic arm capture of space debris using CubeSats represents a viable option if 1) the debris object is initially stable with no angular momentum, and 2) a gripping location exists. If the object begins tumbling after capture, the robotic arm can withstand angular velocities up to $10°/s$ as long as the CubeSat's displacement along the Z-axis is

*Most mass limits are taken from https://earth.esa.int/web/eoportal/satellite-missions/c-missions/cubesat-concept. The $8U$ CubeSat has a 16 kg limit as in [3], and the $16U$ CubeSat is given a 24 kg limitation as in [4].

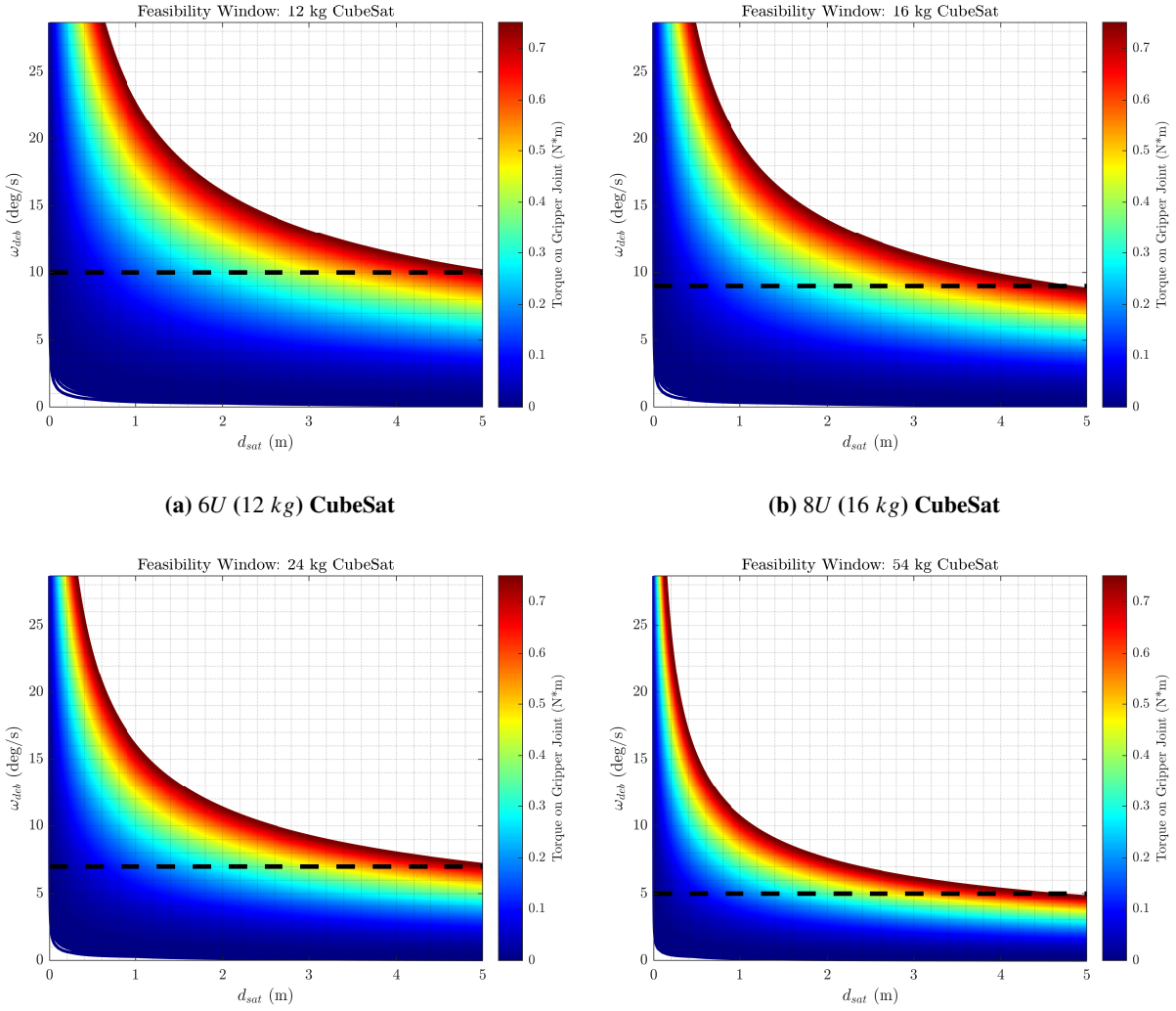

(a) $6U$ $(12\ kg)$ **CubeSat**

(b) $8U$ $(16\ kg)$ **CubeSat**

(c) $12U/16U$ $(24\ kg)$ **CubeSat**

(d) $27U$ $(54\ kg)$ **CubeSat**

Fig. 2 Robotic Arm Torque Feasibility Windows

within 1 m of the debris object's axis of rotation. The angular velocity limit increases even more for CubeSats under 54 kg $(27U)$.

Given the dependence of arm resiliency on accurate knowledge of object angular velocity, identification of the debris object's center of mass should be a priority in robotic arm ADR missions. If the center of mass is incorrectly estimated, not only is d_{sat} likely to increase, but the misaligned thrust imparted by the CubeSat during the deorbit phase will also cause the object to tumble. Moreover, since the debris object must be initially stationary, no conclusions can be drawn about the object's inertia by observing its rotation. Prior knowledge of the debris object's mass properties represents one way to reduce center of mass estimation error for a stationary object.

V. Tethered Rigid Body Dynamics Observation Tool

The harpoon and net capture methods both involve the use of tethers, which leads to complex two-body capture dynamics that are difficult to model analytically. To assist in feasibility analysis, a simulation tool known as the Tethered Rigid Body Dynamics Observation Tool (TeRBoDOT) was developed in MATLAB. This tool uses an Euler numerical method to propagate the motion of a cylindrical debris object in six degrees of freedom and the motion of the CubeSat

in three degrees of freedom. An abbreviated summary of the model is outlined in this section, along with verification cases to quantify the simulation's accuracy.

The CubeSat is modeled simply as a point with mass m_{sat}. Its dynamics are propagated using the following equations:

$$\vec{a}_{sat} = \frac{\vec{F}_{sat}}{m_{sat}} \tag{3}$$

$$\vec{v}_{sat}|_{k+1} = \vec{v}_{sat}|_k + \vec{a}_{sat}\Delta t \tag{4}$$

$$\vec{X}_{sat}|_{k+1} = \vec{X}_{sat}|_k + \vec{v}_{sat}|_k\Delta t + \frac{1}{2}\vec{a}_{sat}\Delta t^2 \tag{5}$$

Where $\vec{F}_{sat}$ represents the net applied force, $\vec{a}_{sat}$ and $\vec{v}_{sat}$ represent acceleration and velocity, and $\vec{X}_{sat}$ represents position. Δt is the propagation time step, and the indices k and $k+1$ denote quantities at the time references t and $t+\Delta t$ respectively.

The rocket body is more complex and is modeled as a rigid body (or more specifically, as a mesh of points arranged in a cylinder to represent the shape of a rigid body). Each point of the cylinder is propagated at each time step using Euler equations of motion for angular rates in addition to equations for linear rates:

$$\dot{\vec{\omega}}_{deb} = I_{deb}^{-1}\left(\vec{\tau}_{deb} - \vec{\omega}_{deb}|_k \times I_{deb}\vec{\omega}_{deb}|_k\right) \tag{6}$$

$$\vec{\omega}_{deb}|_{k+1} = \vec{\omega}_{deb}|_k + \dot{\vec{\omega}}_{deb}\Delta t \tag{7}$$

$$\vec{a}_{deb} = \frac{\vec{F}_{deb}}{m_{deb}} \tag{8}$$

$$\vec{v}_{deb}|_{k+1} = \vec{v}_{deb}|_k + \vec{a}_{sat}\Delta t \tag{9}$$

$$\vec{X}_{deb}|_{k+1} = \vec{X}_{deb}|_k + \vec{v}_{deb}|_k\Delta t + \frac{1}{2}\vec{a}_{deb}\Delta t^2 \tag{10}$$

In the angular motion equation, $\vec{\omega}_{deb}$ indicates debris object angular velocity, $\vec{\tau}_{deb}$ represents applied torques, and I_{deb} represents the principal inertia matrix. The angular rates are applied to the series of debris object points using Euler rotation matrices. By repeatedly evaluating the propagation equations for both object and CubeSat in response to applied forces, the TeRBoDOT simulation propagates through a four-stage capture scenario:

1) Harpoon or net firing: The harpoon or net is fired at the debris object, and penetrates or entangles it (respectively).
2) Delay: A brief delay of 1 s is implemented between harpoon/net firing and tether tensioning. This pause allows for the winding mechanism to pull the tether taut. If the relative velocity between the CubeSat and debris object causes the tether to pull taut before 1 s has elapsed, winding begins at that moment instead due to the absence of slack.
3) Winding: The tether is wound in with a constant force. Depending on the motion of the objects, the winding force may either act to accelerate the two objects' movement towards one another, or to dampen and reduce their motion away from each other.
4) Feasibility analysis: A final feasibility decision is obtained by repeatedly evaluating a series of constraints, including acceleration limitations, collision analysis, and approach speed, until one is violated or all are satisfied. Once a constraint violation or full constraint satisfaction occurs, the scenario is marked as either feasible or infeasible as appropriate.

To better visualize the TeRBoDOT simulation (and simplify anomaly detection), a plot of the simulation progress is produced and written to a GIF file with each time step. Sample plots are shown in Figure 3, which shows example simulations at two different points after harpoon or net firing.

Three series of analytically verified test cases are used to establish the accuracy of the model and quantify its errors. In all these cases, the simulation is started with the two objects already connected instead of at the moment of harpoon or net firing. This modification enables precise specification of the two objects' initial positions and velocities, which

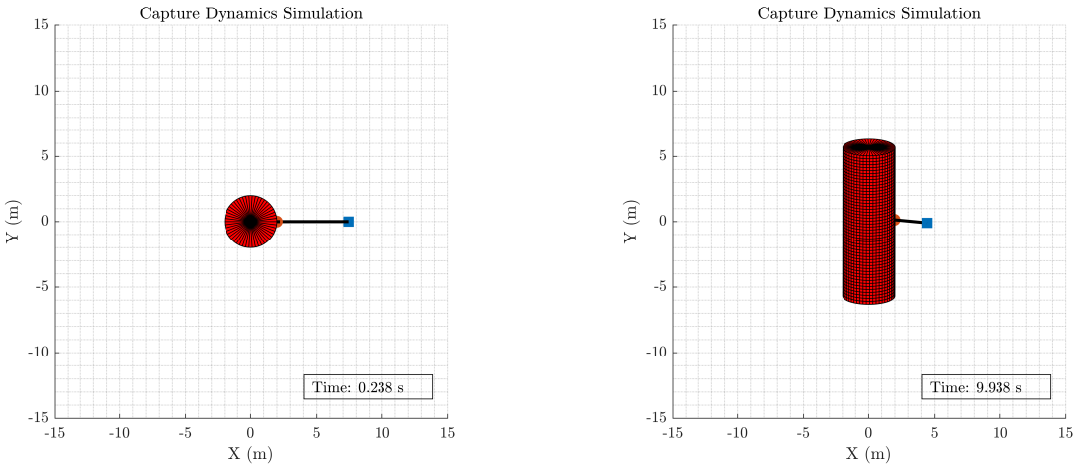

(a) $t \approx 0\ s$ **(b)** $t \approx 10\ s$

Fig. 3 TeRBoDOT Simulation Examples

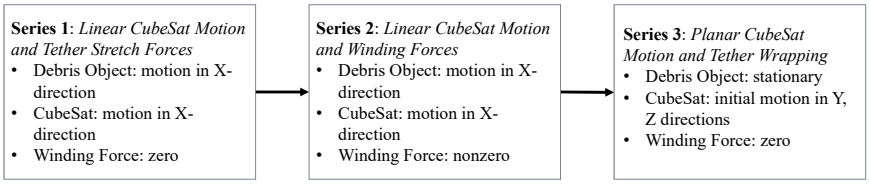

Fig. 4 TeRBoDOT Verification Process

would otherwise be affected by forces exerted during the firing event. The debris object is assumed to have a diameter of 4 m and a length of 10 m, and the tether has a length of 5 m except where otherwise stated.

Figure 4 shows the testing process and the primary emphasis areas for each test series. The goal of Series 1 is to assess the performance of the model in simulating cases involving linear motion where the tether becomes stretched. In Series 1, the debris object and CubeSat are given positions and initial velocities along the X-axis (the same configuration shown in Figure 3a). Relative velocities are assigned such that the CubeSat's motion will eventually pull the tether to its full length, causing the CubeSat and debris objects to recoil towards one another and eventually come into contact. Winding force is set equal to zero to ensure the only force acting between the two objects is imparted by the stretched tether. Series 2 is designed to examine the performance of the simulation when applying a winding force instead of a tether stretch force. The series is executed in a similar way to Series 1, except that winding force is now nonzero. The debris object begins at rest, and the CubeSat is given a linear velocity along the X-axis. Due to the winding force, the tether is never pulled to its full length, meaning that any stretching experienced by the tether is negligible. Series 3 examines the performance of the simulation when the tether wraps around the debris object. With the tether fully extended, the CubeSat receives an initial velocity in the YZ-plane. Winding force is set equal to zero, and the debris object is kept stationary at the origin throughout the simulation. For Series 1-3, the quantities examined are the time the two objects come into contact (t_{col}) and/or the location where this event occurs (X_{col}). Analytical calculations (assumed to be truth data) are compared with TeRBoDOT results, and percent error is calculated. Together, Series 1-3 provide insight into the model's propagation accuracy for three different types of events. In any given harpoon or net capture simulation, any or all of these events could be encountered.

Four test cases are chosen for Series 1. The debris object and CubeSat both start with initial velocities ($v_{sat}|_{t_0}$ and $v_{deb}|_{t_0}$ and positions ($X_{sat}|_{t_0}$ and $X_{deb}|_{t_0}$) along the X-axis, and the tether is initially slack. In order to simulate a range of input conditions, the CubeSat and debris object both have different masses (m_{sat} and m_{deb}) and initial velocities for each test case. The tether attachment point is centered on the debris object, and winding force is set equal to zero. The two bodies' initial velocity eventually induces tension in the elastic tether, causing the objects to recoil toward one

another. Simulation parameters for each of the four cases are shown in Table 2.

Table 2 TeRBoDOT Linear Momentum Test Cases

	CubeSat			Debris Object		
Number	m_{sat} (kg)	$X_{sat}\|_{t_0}$ (m)	$v_{sat}\|_{t_0}$ (m/s)	m_{deb} (kg)	$X_{deb}\|_{t_0}$ (m)	$v_{deb}\|_{t_0}$ (m/s)
1	12	1	0.1	500	0	0
2	16	2	0.2	1,000	0	0.1
3	24	3	0.25	100	0	0.05
4	54	4	0.3	750	0	0.15

Conservation of energy and linear momentum principles enable analytic calculation of how long the CubeSat and debris object will take to come into contact with one another (t_{col}), as well as the linear position along the X-axis at which this event will occur (X_{col}). These calculations are compared with the results of the simulation, and percent error is computed for each case. The equations used for analytic calculations are summarized below. Determining t_{col} and X_{col} begins with defining t_{taut}, the time at which the tether pulls tight between the CubeSat and debris object:

$$t_{taut} = \frac{X_{deb}|_{t_0} - X_{sat}|_{t_0} + l_{tether}}{v_{sat}|_{t_0} - v_{deb}|_{t_0}} \tag{11}$$

After time t_{taut}, the CubeSat and debris object recoil towards one another with velocities $v_{sat}|_{t_1}$ and $v_{deb}|_{t_1}$, respectively. These two quantities are calculated simply by equating linear momentum and kinetic energy both before and after t_{taut}, and solving for $v_{sat}|_{t_1}$ and $v_{deb}|_{t_1}$ in terms of m_{sat}, m_{deb}, $v_{sat}|_{t_0}$, and $v_{deb}|_{t_0}$. From these quantities, the analytic expressions, X_{col} and t_{col} are computed as:

$$X_{col} = (X_{deb}|_{t_0} + v_{deb}|_{t_0} t_{taut}) + v_{deb}|_{t_1} \left(\frac{(X_{sat}|_{t_0} + v_{sat}|_{t_0} t_{taut}) - (X_{deb}|_{t_0} + v_{deb}|_{t_0} t_{taut})}{(v_{deb}|_{t_1} - v_{sat}|_{t_1})} \right) \tag{12}$$

$$t_{col} = t_{taut} + \left(\frac{(X_{sat}|_{t_0} + v_{sat}|_{t_0} t_{taut}) - (X_{deb}|_{t_0} + v_{deb}|_{t_0} t_{taut})}{(v_{deb}|_{t_1} - v_{sat}|_{t_1})} \right) \tag{13}$$

Table 3 illustrates the results of the four test cases outlined in Table 2. The percent error for both X_{col} and t_{col} is 10-16% and is calculated by comparing the analytic result to the corresponding TeRBoDOT result for each case (assuming the analytic result represents the actual value). It is observed that higher mass CubeSats produce smaller test errors, a behavior that is explained by the simulation's time step. Larger CubeSats cause the tether to stretch further and over a longer duration, while small CubeSats only generate a momentary stretch. The latter case is more difficult to simulate accurately with a fixed time step, and often leads to overestimation of the reaction force. While larger CubeSats experience the same kind of error, the effect is less pronounced due to the longer duration of the stretch event relative to the time step. This behavior is an inherent limitation of the numerical method and can be reduced by shortening the time step. In this case, however, computational limitations rendered a smaller step impractical.

Table 3 TeRBoDOT Linear Momentum Test Results

	Analytic		TeRBoDOT			
Number	X_{col} (m)	t_{col} (s)	X_{col} (m)	t_{col} (s)	% Error (X_{col})	% Error (t_{col})
1	0.2344	90	0.2	75.35	14.68	16.28
2	8.1575	80	6.8421	67.05	16.13	16.19
3	3.6855	35	3.1951	29.45	13.31	15.86
4	6.6716	40	5.9919	35.75	10.19	10.63

Series 2 contains four additional test cases, in which the debris object begins at rest at the origin while the CubeSat is allowed to have nonzero initial velocity. In these cases, the delay in winding is skipped, and the winding force is applied beginning at $t = 0\ s$. The simulation parameters for this test series are shown in Table 4. To diversify the initial conditions, each case has unique values for CubeSat and debris object mass, CubeSat initial position, CubeSat initial velocity, and winding force. Like Series 1, analytic calculations for t_{col} and X_{col} are compared with TeRBoDOT results to compute percent error. The equations used to determine analytic solutions for each test case are:

$$X_{sat}|_{t_0} + v_{sat}|_{t_0} t_{col} + \frac{1}{2}\left(\frac{-F_{winding}}{m_{sat}}\right) t_{col}^2 - \left(v_{deb}|_{t_0} t_{col} + \frac{1}{2}\left(\frac{F_{winding}}{m_{deb}}\right) t_{col}^2\right) = 0 \tag{14}$$

$$X_{col} = X_{sat}|_{t_0} + v_{sat}|_{t_0} t_{col} + \frac{1}{2}\left(\frac{F_{winding}}{m_{sat}}\right) t_{col}^2 \tag{15}$$

The first equation is solved for t_{col} in terms of the variables shown in Table 4. X_{col} is then determined using the same variables and the value calculated for t_{col}.

Table 4 TeRBoDOT Winding Test Cases

Number	m_{sat} (kg)	m_{deb} (kg)	F_{sat} (N)	$X_{sat}\|_{t_0}$ (m)	$v_{sat}\|_{t_0}$ (m/s)
5	12	1,500	0.05	1	0.1
6	16	1,000	0.1	1.5	0.05
7	24	750	0.5	3	-0.05
8	54	500	1.0	4.5	0

Table 5 TeRBoDOT Winding Test Results

	Analytic		TeRBoDOT			
Number	X_{col} (m)	t_{col} (s)	X_{col} (m)	t_{col} (s)	% Error (X_{col})	% Error (t_{col})
5	0.0525	56.11	0.0525	56.15	0	0.07
6	0.0480	30.99	0.0480	31	0	0.03
7	0.0705	14.54	0.0706	14.55	0.14	0.07
8	0.4386	20.94	0.4389	20.95	0.07	0.05

Table 5 shows the results of Series 2. As in Series 1, analytic calculations are compared with TeRBoDOT results and percent error is computed. Unlike the first series, the tether winding cases do not impart a sudden stretch on the tether, thus avoiding the error discussed in the previous set of test cases. The results of this second set of cases match quite closely with analytical calculations, and no errors exceed 0.15%.

Series 3 is designed to evaluate the accuracy of the simulation in cases where the tether wraps around the debris object. Because MATLAB does not readily allow for the construction of rigid bodies that detect CubeSat collisions or tether wraps, the surface of the debris object is modeled instead as a series of interconnected nodes. The wrapping behavior of the tether (with length l_{tether}) is therefore constrained by node positions and cannot always follow a smooth curve. These cases quantify the errors introduced by that design limitation. All scenarios begin with the tether taut but not stretched, and no winding force is applied to the tether. The CubeSat starts along the X-axis and is given an initial velocity in the YZ-plane, causing it to swing around its attachment point by 90° and then wrap around the debris object, which is held motionless at the origin. The angle of wrap depends on the direction of initial velocity. To simplify notation, initial CubeSat velocity is defined parametrically using a magnitude v_0 and an angle θ_v. θ_v is measured about the X-axis, with $\theta_v = 0$ lying in the XY-plane:

$$\vec{v}_0 = < 0, v_0 cos(\theta_v), v_0 sin(\theta_v) > \tag{16}$$

An angle of $\theta_v = 0°$ corresponds to an initial velocity in the XY-plane that causes the tether to wrap around the circumference of the cylinder. $\theta_v = 90°$ indicates a velocity in the XZ-plane, which tends to wrap around the end of the cylinder (or strike the object near one end if the tether is short).

t_{col}, the time required for the CubeSat to wrap around the debris object and come into contact with its surface, is compared for analytic calculations and TeRBoDOT. The analytic values are determined using the equation below[†]

$$t_{col} = \frac{\pi l_{tether}}{2v_0} + \frac{l_{tether}^2 cos(\theta_v)}{2r_{deb}v_0} \tag{17}$$

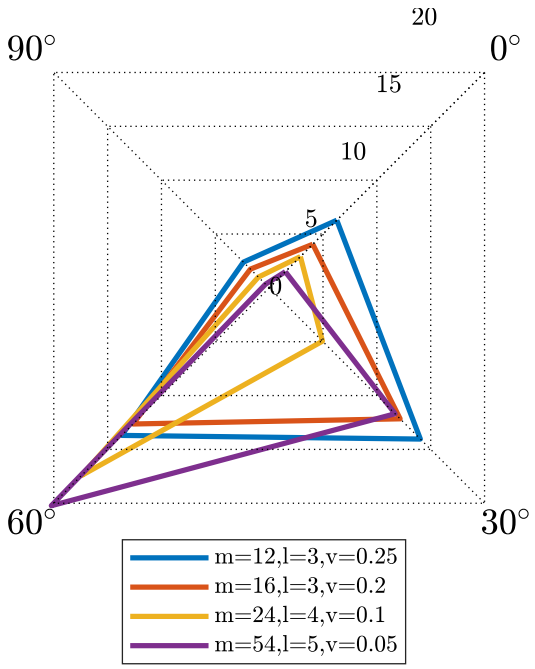

Fig. 5 TeRBoDOT Tether Wrapping Test Cases

Figure 5 shows a comparison between TeRBoDOT predictions and analytically determined values for t_{col}. In the radar plot, the radial direction shows percent error and is calculated assuming the analytic calculations represent truth data. The angular measurements marked at each vertex of the plot represent θ_v. The legend indicates the parameters used for each test case: CubeSat mass in kg, tether length in m, and initial velocity in m/s. Because the points representing the debris object's surface are connected to one another at 0°, 45°, and 90° angles (each node is connected to its neighbors vertically, horizontally, and diagonally), simulations involving these angles can be estimated the most precisely. The test cases using one of these angles all have errors below 10%. Intermediate angles such as 30° and 60° lead to higher errors between 10-20%. At these angles, the tether is forced to follow a less precise trajectory estimate because the node connections do not naturally conform to the desired tether wrap angle.

To better visualize the effect of wrapping angle on tether path, Figure 6 presents the results of two simulations involving tether wrapping. Figure 6a shows a 45° wrapping angle, which naturally conforms to the connections between nodes. Figure 6b shows a 60° wrapping angle. In this second case, it is clear that the limitations on node connections restrict the ability of the simulated tether to closely match the idealized path.

The TeRBoDOT simulation is applied to both harpoon and net capture in the upcoming sections, where it is used to estimate success probabilities for different capture scenarios. Besides concerns about dynamic stability and collisions between the CubeSat and debris object, both methods also have their own unique requirements regarding aim accuracy and firing velocity.

[†]A portion of Equation 17 is taken from a derivation on the Physics Stack Exchange website, https://physics.stackexchange.com/questions/313021/a-rope-wrapping-around-a-cylinder.

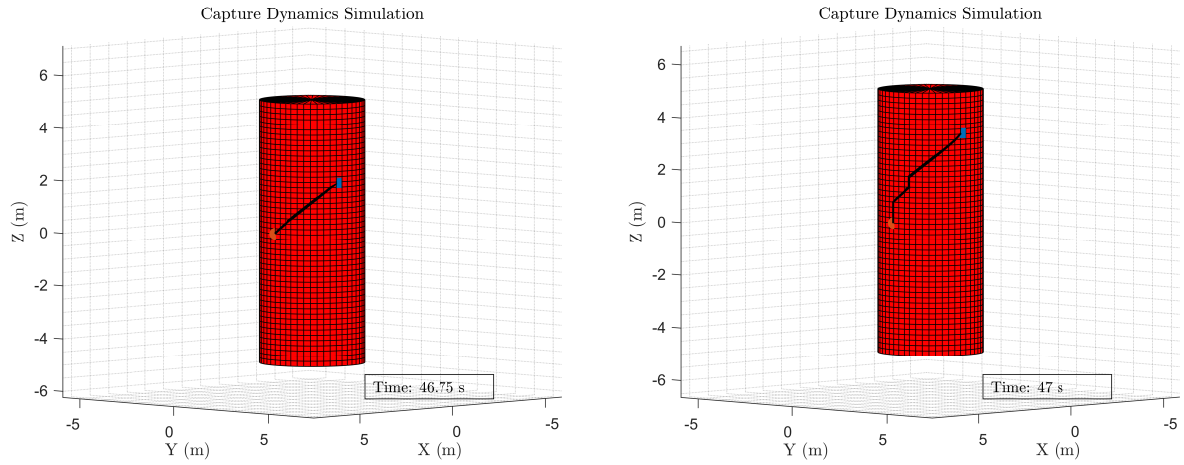

(a) 45° **Wrapping Angle** **(b)** 60° **Wrapping Angle**

Fig. 6 Estimated Tether Paths at 45° **and** 60° **Wrapping Angles**

VI. Harpoon Capture

While robotic arm capture requires separation of less than a meter between the CubeSat and debris object, harpoon capture is initiated at a distance of several meters from the object. Additionally, it is not limited to stationary debris objects by the requirement for motion synchronization, and no designated grapple feature is necessary. As long as the harpoon is traveling fast enough to penetrate the debris object's sidewall, a wide variety of locations suffice.

The harpoon method's concept of operations begins with the CubeSat establishing a position in proximity to the debris object and characterizing its motion using onboard sensors. Rather than the centimeter-scale separation required by the robotic arm, this observation phase might take place at a distance of several tens of meters. Once the motion has been mapped, the CubeSat maneuvers to within a few meters of the object and uses its ADCS to aim the harpoon. The harpoon projectile is then fired at the intended contact point. If the attempt is successful, the harpoon punctures the side of the debris object and deploys a barb, establishing a secure manipulation point on the object's surface. The CubeSat then winds in the tether, pulling itself alongside the object. Once winding is complete, functions such as detumbling and deorbiting commence. The following subsections analyze key steps of the harpoon capture process in chronological order, beginning with a discussion of the precision needed for aiming the harpoon and concluding with estimations of success probability for different winding and docking scenarios.

A. Aim and Incidence Angle

The initial parameters of a capture scenario are shown in Figure 7. The CubeSat's position is defined as $\vec{X}_{sat}$ and is measured relative to the debris object's center of mass. $\vec{X}_{sat}$ is contained in a box with dimensions $[X_{box}, Y_{box}, Z_{box}]$, used to model the satellite's position uncertainty at the instant of firing. Two angles, yaw (ψ) and pitch (ϕ), define the pointing attitude of the CubeSat and are illustrated in Figures 7a and 7b. For the harpoon to strike the debris object, it must be true that $\psi_{min} \leq \psi \leq \psi_{max}$ and $\phi_{min} \leq \phi \leq \phi_{max}$. Incidence angle, α, is defined as the minimum angle between the harpoon's velocity vector and a tangent plane to the debris object's surface at the point of impact. The pitch and yaw components of incidence angle (α_{XZ} and α_{XY}), from which the overall incidence angle is derived, are shown in Figure 7c. A high incidence angle maximizes normal force and increases the likelihood of a successful penetration. Equations for ϕ_{min}, ϕ_{max}, ψ_{min}, ψ_{max}, and α are presented below:

$$\phi_{min} = \pi - tan^{-1}\left(\frac{-\vec{X}_{sat}(3) + l_{deb}/2}{\sqrt{|\vec{X}_{sat}(1)|^2 + |\vec{X}_{sat}(2)|^2} - D_{deb}/2}\right) \tag{18}$$

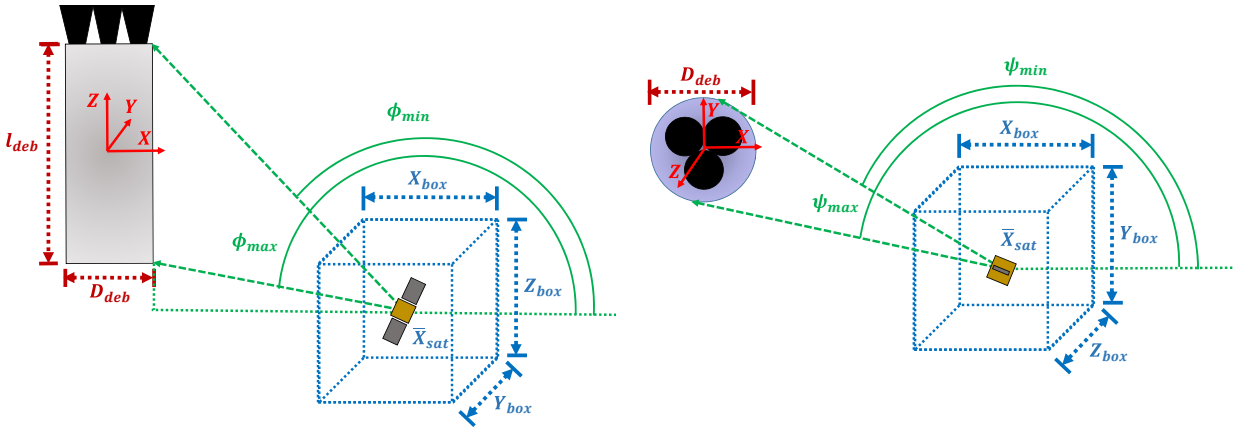

(a) Side View

(b) Top View

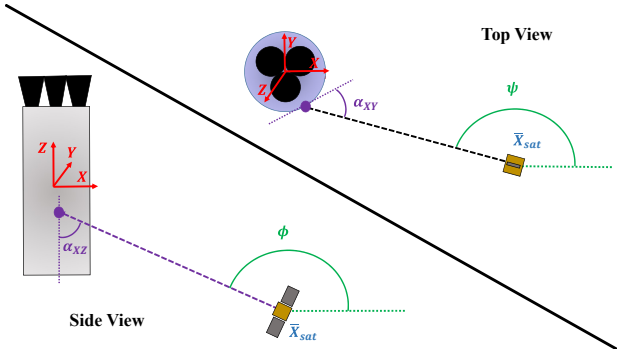

(c) Pitch, Yaw, and Incidence Angles

Fig. 7 Harpoon Scenario Targeting Diagrams

$$\phi_{max} = \pi - tan^{-1}\left(\frac{-\vec{X}_{sat}(3) - l_{deb}/2}{\sqrt{|\vec{X}_{sat}(1)|^2 + |\vec{X}_{sat}(2)|^2} - D_{deb}/2}\right) \tag{19}$$

$$\theta_{yaw} = \pi - tan^{-1}\left(\frac{-\vec{X}_{sat}(2)}{\vec{X}_{sat}(1)}\right) \tag{20}$$

$$\psi_{min} = \theta_{yaw} - sin^{-1}\left(\frac{D_{deb}/2}{\sqrt{|\vec{X}_{sat}(1)|^2 + |\vec{X}_{sat}(2)|^2}}\right) \tag{21}$$

$$\psi_{max} = \theta_{yaw} + sin^{-1}\left(\frac{D_{deb}/2}{\sqrt{|\vec{X}_{sat}(1)|^2 + |\vec{X}_{sat}(2)|^2}}\right) \tag{22}$$

$$\alpha_{YZ} = \frac{\pi}{2} - |\pi - \phi| \tag{23}$$

$$\alpha_{XY} = cos^{-1}\left(\frac{\sqrt{\vec{X}_{sat}(1)^2 + \vec{X}_{sat}(2)^2}\, sin(|\psi - \theta_{yaw}|)}{D_{deb}/2}\right) \tag{24}$$

$$\alpha = tan^{-1}\left(\frac{1}{\sqrt{\frac{1}{tan(\alpha_{XY})^2} + \frac{1}{tan(\alpha_{YZ})^2}}}\right) \tag{25}$$

Monte Carlo simulation is used to predict the likelihood of striking a debris object at different incidence angles given uncertainty in both CubeSat position and pointing direction. Three objects with different dimensions are used as case studies, and each is considered with two different levels of CubeSat position uncertainty. In every case, this uncertainty is represented by a symmetric box about the CubeSat as shown in Figures 7a and 7b. A less uncertain scenario has a smaller position box, indicating the position is better known. The position box is centered on the +X axis at a specified capture distance, measured from the debris object's surface. For each case study, the CubeSat is assumed to have a 1σ pointing accuracy of 2°, a capability demonstrated by the $3U$ CanX-2 CubeSat [5]. The actual pitch and yaw angles are modeled as normal distributions about the centers of their respective ranges. The three case studies considered are:

1) SL-16 rocket body (12 $m \times 4$ m dimensions)
2) SL-8 rocket body (6 $m \times 2$ m dimensions, [6])
3) Small cylindrical debris (1 $m \times 0.5$ m dimensions)

Each case study is considered at a 5 m capture distance, a representative value for the harpoon CONOPS. The position box is 1 $m \times 1$ $m \times 1$ m. 100,000 runs are performed for each case study, with the CubeSat's position randomly distributed throughout the scenario's position box and the pointing accuracy normally distributed with $\sigma = 2°$. In each run, required pointing stability is calculated using Equations 18 through 22. Specific values for pitch and yaw are selected using the pointing accuracy distribution, and the resulting incidence angle is calculated using Equation 25. In aggregate, each set of runs provides an overview of the pitch and yaw stability required for the respective case study, along with a distribution of incidence angles.

A majority of the trials result in angles of incidence greater than 45° across all the case studies. The empirically determined probabilities of different outcomes are outlined in Table 6, with each row of the table corresponding to one of the case studies. $P(hit)$ represents the probability of striking the object in each case study, while $P(\alpha \geq \theta)$ denotes the probability of also achieving an incidence angle higher than θ. The 2° pointing accuracy proves sufficient to ensure the harpoon strikes the object at least 80% of the time for each case study, and results suggest at least a 50% chance of striking with an incidence angle higher than 60°. As object size decreases, however, the probability of obtaining an incidence angle greater than 80° falls as low as 18%. One way to account for lower incidence angles is by increasing the harpoon firing velocity. The structural limits of CubeSats with respect to firing speed and debris object thickness are treated in the next section.

Table 6 Harpoon Capture Event Probabilities, %

Debris Object	$P(hit)$	$P(\alpha \geq 45°)$	$P(\alpha \geq 60°)$	$P(\alpha \geq 80°)$
SL-16	100.00	100.00	100.00	83.16
SL-8	100.00	99.93	98.22	56.85
Small Cylinder	82.40	66.19	50.00	17.26

The trials that struck the target (included in $P(hit)$) are plotted in Figures 8 through 10. In the left series of plots, the X-axis represents required yaw stability (maximum angular deviation from the midpoint of the yaw range without missing the debris object) and the Y-axis represents required pitch stability. The maximum and minimum values are representative of the required pointing precision needed to ensure impact. For example, Figure 8 indicates that depending on the CubeSat's location in the position box, required yaw stability is $15.4 - 17.9°$ and required pitch stability is $47.3 - 53.1°$. The colored points illustrate the incidence angle for each run. Because the large number of trials makes it difficult to identify the various colors of the points, the plots on the right present histograms to show the distribution of incidence angles more clearly.

B. Harpoon Deployment

The results described in the previous section suggest that with a pointing accuracy of 2° or less, a CubeSat has at least a 50% probability of striking the debris object at an incidence angle of 60° or greater, even with positioning

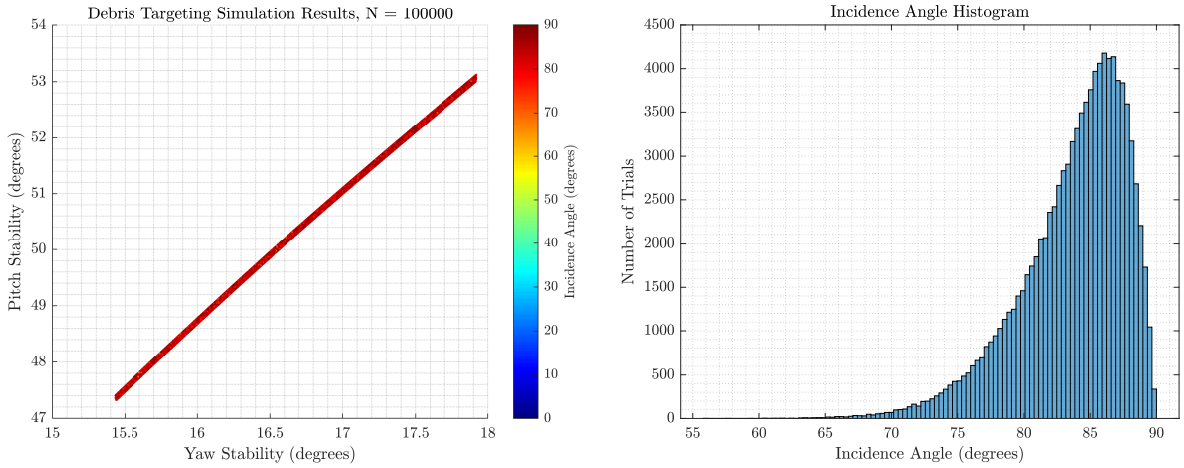

(a) Yaw and Pitch Stabilities **(b) Incidence Angles**

Fig. 8 SL-16 Rocket Body Targeting Simulation, 5 m Distance

uncertainty on the order of meters. This conclusion was true across all of the case studies examined. However, striking the object does not necessarily equate to a successful capture: the harpoon must also have sufficient velocity to ensure penetration of the surface. At the same time, firing the harpoon must not cause the CubeSat to experience an excessive recoil acceleration on firing. Sensitive components such as deployed solar arrays may be damaged if the recoil acceleration is too great. This section explores the relationship between object surface thickness, incidence angle, and firing acceleration experienced by the CubeSat.

Assuming the debris object has an outer shell with thickness T_{deb}, the minimum impact force F_{min} needed to ensure successful penetration can be expressed as the product of material shear strength, s_{deb}, and shear area, A_s:

$$F_{min} = s_{deb} A_s = s_{deb} \left(T_{deb} p\right) \tag{26}$$

Where p is the perimeter of the shear area, estimated as an ellipse with the Selmer II approximation[‡]: $p \approx \left(\frac{\pi}{4}\right)\left(\left(6 + \frac{1}{2}\frac{(a_1-b_1)^2}{(a_1+b_1)^2}\right)(a_1+b_1) - \sqrt{2(a_1^2+3a_1b_1+b_1^2)}\right)$. In the expression for p, $a_1 = \frac{D_{hole}}{2sin(|\alpha|)}$ and $b_1 = \frac{D_{hole}}{2}$, with α representing incidence angle. D_{hole} indicates the diameter of the projectile tip.

Actual impact force (whether sufficient for penetration or not) can be expressed using conservation of energy by dividing the projectile's kinetic energy by the distance of penetration. This calculation assumes the harpoon is completely stopped by the debris object, and that all the the kinetic energy is transferred into the debris surface as a normal force. The resulting equation is:

$$F_{imp} = \frac{\frac{1}{2} m_{proj} v_{imp}^2 sin(|\alpha|)}{T_{deb}} \tag{27}$$

Where F_{imp} represents impact force, m_{proj} is harpoon mass, and v_{imp} is the harpoon's impact velocity. By setting $F_{min} = F_{imp}$, the minimum v_{imp} needed by the projectile to puncture the object can be determined if the object characteristics (material properties and thickness) and harpoon specifications (mass and tip diameter) are known. The incidence angle must also be a known quantity.

A case study is performed to determine the maximum thickness a CubeSat can penetrate, assuming the object's outer shell is composed of 6061-T6 aluminum alloy[§]. The harpoon mass and diameter are modeled after the only flight-proven harpoon payload, that of the RemoveDebris mission. Accordingly, harpoon mass is 0.115 kg, tip diameter is 1 cm, and deployment tube length is 0.15 m [7][8]. To avoid damage to the CubeSat, which by this point in the mission has

[‡]See "Approximations of Ellipse Perimeters and of the Complete Elliptic Integral E(x). Review of known formulae" by Stanislav Sŷkora, http://www.ebyte.it/library/docs/math05a/EllipsePerimeterApprox05.html.

[§]Reference MatWeb, "Aluminum 6061-T6; 6061-T651", http://www.matweb.com/, for aluminum material properties.

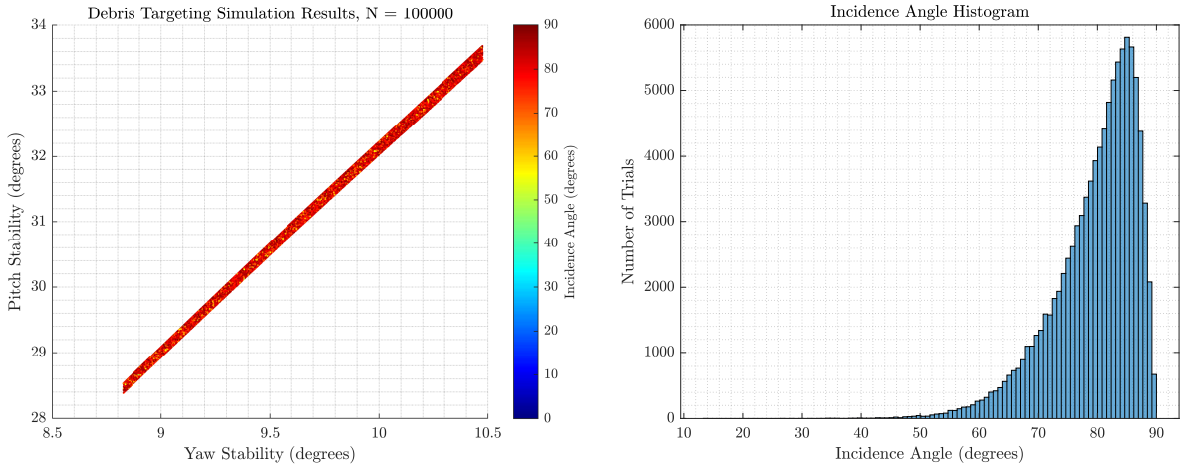

(a) Yaw and Pitch Stabilities **(b) Incidence Angles**

Fig. 9 SL-8 Rocket Body Targeting Simulation, 5 m Distance

deployed its solar arrays, the recoil acceleration imparted on the CubeSat must not exceed the maximum allowable limit of 1 G (a design limit driven by the acceleration experienced during docking [9]). The acceleration constraint translates to the following statement:

$$\frac{m_{proj} a_{firing}}{m_{sat}} \leq 1G \tag{28}$$

Where $a_{firing} = \frac{v_{firing}^2}{2d_{firing}}$. In this case study, the debris object and CubeSat are both presumed stationary such that $v_{firing} = v_{imp}$. Using equations 26, 27, and 28, the maximum firing velocity sustainable for a 12 kg CubeSat is 17.5 m/s. The maximum velocity increases to 20.2 m/s for a 16 kg CubeSat, 24.8 m/s for a 24 kg CubeSat, and 37.2 m/s for a 54 kg CubeSat.

Figure 11 is constructed to show the region in which the acceleration constraint is satisfied and the object is penetrated for different values of T_{deb} and α. Four different CubeSat sizes are examined. In each plot, the shaded area represents the feasible capture region for a CubeSat of that mass, with the colorbar indicating the acceleration imparted on the CubeSat during firing (limited to 1 G). It is clear that in all cases, an increase in incidence angle (i.e. a more direct impact) allows a thicker object to be penetrated, since the puncture area is minimized when $\alpha = 90°$. At maximum incidence angle, a 12 kg CubeSat is capable of puncturing a sidewall with a thickness of roughly 1.6 mm. That number increases to 1.8 mm for a 16 kg CubeSat, 2.2 mm for a 24 kg CubeSat, and 3.3 mm for a 54 kg CubeSat. Given the parameters used in this case study, any object thicker than these limits cannot be successfully penetrated with the harpoon without overstressing the CubeSat. Further study is needed to determine the required barb diameter and design to ensure the harpoon remains lodged in the debris object and cannot pull loose. In this work, a successful harpoon penetration is assumed to remain anchored in the debris object without loosening.

The penetration capabilities of a harpoon-equipped CubeSat are likely to have utility among existing debris objects. The thicknesses of rocket bodies vary, and specifications are not necessarily publicly available. However, the average tank thickness across five US rocket stages for which data is available (Agena, Atlas, Centaur, Saturn IV, and Titan) is 1.7 mm [10], a value that falls in the feasible range for three out of the four CubeSat sizes examined in Figure 11. The same source also indicates that three of the five stages are composed of an aluminum alloy, as was assumed in this section. A fraction of the rocket bodies currently on orbit could therefore represent feasible harpoon capture targets, especially those that lack additional insulating layers covering the tank wall.

C. Winding and Docking

The previous sections have concluded that a harpoon can successfully strike various debris objects given existing CubeSat pointing capabilities. It has also been shown that a harpoon-based capture method can penetrate the object,

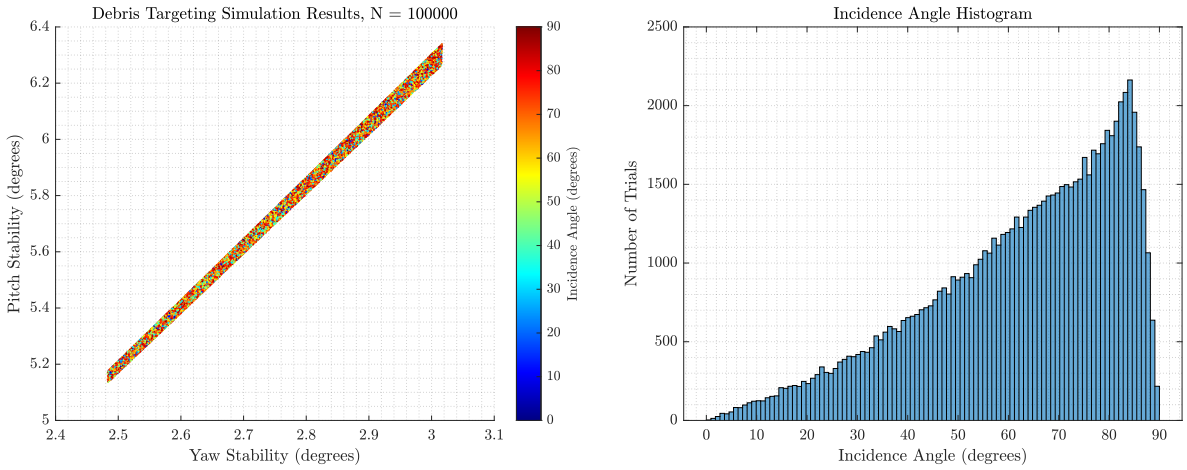

(a) Yaw and Pitch Stabilities **(b) Incidence Angles**

Fig. 10 Small Cylindrical Debris Targeting Simulation, 5 m **Distance**

provided the sidewall thickness is less than $2-3\ mm$ for an aluminum object. To achieve success, though, the CubeSat must not only target and penetrate the debris object, but also wind in its tether and successfully arrive at the point of harpoon impact. Meanwhile, it must avoid colliding with the object (striking the object's surface away from the harpoon impact location), snapping its tether, or undergoing rapid accelerations that could threaten sensitive components such as deployed solar arrays.

Using the TeRBoDOT simulation, harpoon capture feasibility envelopes are identified across a range of CubeSat sizes and debris object masses. For consistency in debris object characteristics, analytic relationships between object dry mass and overall dimensions are used in this work. Debris object radius is assumed to be proportional to the square root of mass, and height in turn is proportional to radius. Use of a square root instead of a cube root relationship between mass and radius allows the density of the object to decrease as dry mass increases. This assumption reflects the expectation that massive debris objects are typically spent upper stages with a high percentage of empty volume, while smaller objects may be payloads or fragmentary debris with greater density. The Zenit second stage rocket body has known dimensions (12 m length and 4 m diameter) and mass ($8,900\ kg$) [6], and its parameters are used to calibrate the expressions for debris object dimensions. The radius of a particular object is represented by:

$$r_{deb} = 2\sqrt{\frac{m_{deb}}{8900}} \tag{29}$$

And the length is related to the radius as:

$$l_{deb} = 6r_{deb} \tag{30}$$

Both quantities are measured in meters. r_{deb} and l_{deb} are plotted together versus debris object mass in Figure 12. In all feasibility analyses presented in this chapter, debris object dimensions are sized according to these relationships, with mass varying between $100-10,000\ kg$. An additional curve is plotted to show the assumed object density as a function of mass, measured as a multiple of the Zenit rocket body's overall density. Since the Zenit has an overall density of 59 kg/m^3, an object with a mass of 100 kg has a density 9.5 times that of the Zenit (561 kg/m^3). The relative density ratio passes through 1 exactly at the Zenit's mass point, which is marked with a dotted black line.

For all harpoon capture simulations in this section, the tether is assumed to be half as long as the debris object. If the CubeSat approaches to distance less than approximately half the object's length, it risks being struck by the debris object prior to initiating capture if the angular velocity has been incorrectly estimated. On the other hand, increasing capture distance extends the winding process and magnifies the destabilizing effect of the debris object's rotation. A tether length equal to half the object's length therefore represents a balance between minimizing capture distance and maintaining a safe degree of separation before initiating capture. For objects between 100 kg and $10,000\ kg$,

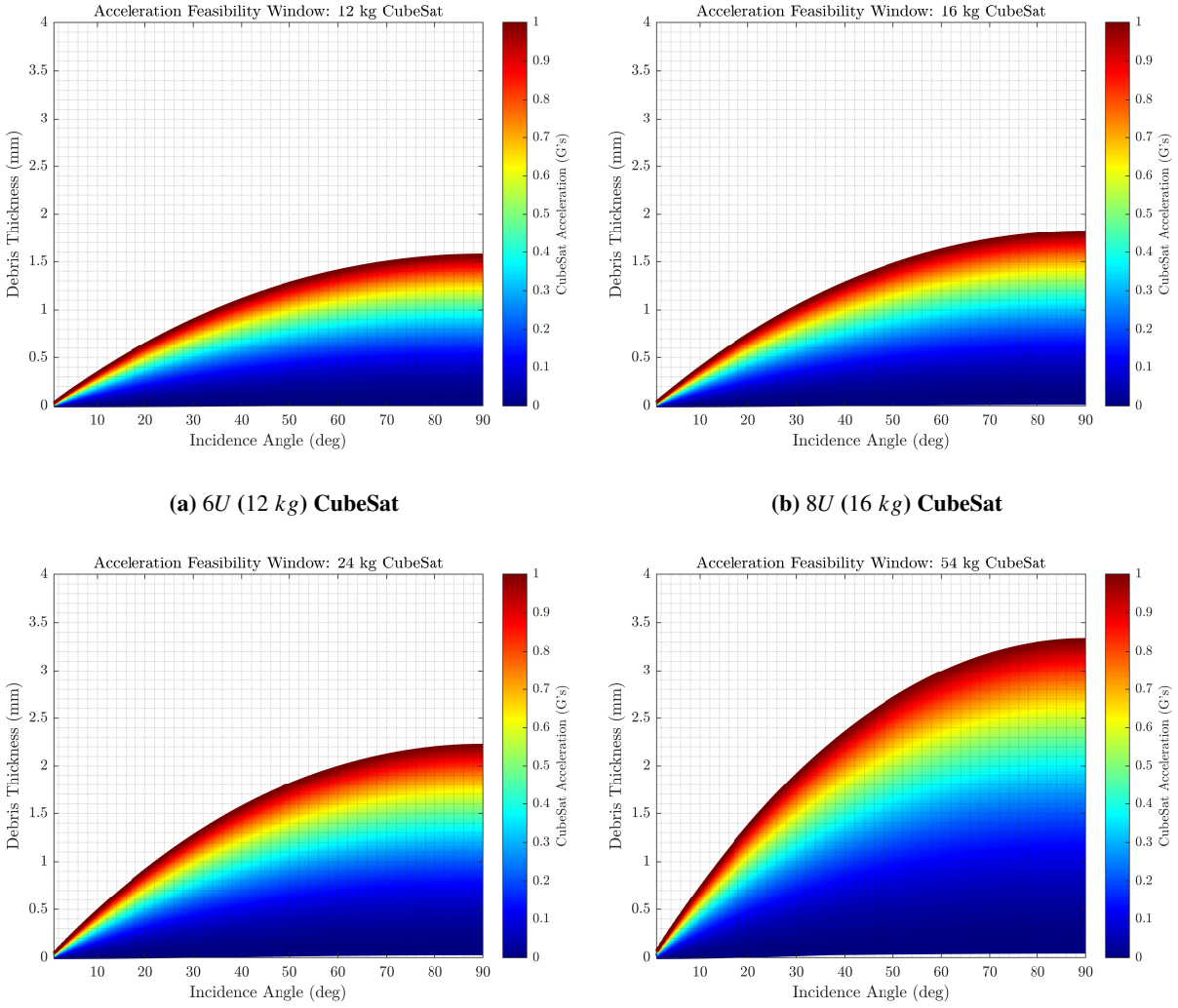

(a) $6U$ $(12\ kg)$ **CubeSat**

(b) $8U$ $(16\ kg)$ **CubeSat**

(c) $12U$/$16U$ $(24\ kg)$ **CubeSat**

(d) $27U$ $(54\ kg)$ **CubeSat**

Fig. 11 Harpoon Firing Acceleration Feasibility Windows

this relationship translates to tether lengths of 0.6 m to 6.4 m. This assumption of variable tether length might be implemented in real life by installing a tether considerably longer than the expected capture distance, and then only allowing deployment of a portion of the tether as dictated by the mission. In all cases, the CubeSat's capture distance is equal to $0.9 * l_{tether}$, measured from the debris object's surface. To account for uncertainty, the CubeSat is also given a position adjustment in the range of $\pm 0.1 l_{tether}$ m and a velocity adjustment (from rest) in the range ± 0.05 m/s along each of the three coordinate axes. Note that the relationship between position error and tether length assumes increasing precision with decreasing distance. The debris object is given an initial angular velocity in the range of ± 0.025 rad/s, or $\pm 1.4°/s$ in each axis. All values are uniformly selected from the indicated ranges for CubeSat position, CubeSat velocity, and object angular velocity for each simulation run.

To vary simulation parameters such as object thickness and winding tension in a cohesive but computationally feasible manner, two sets of harpoon capture simulations are performed. The two sets are shown in Table 7. The first assumes a 1 mm thick debris object with a harpoon firing velocity of 15 m/s. As discussed in Section VI.B, all four of the CubeSat sizes examined are capable of penetrating a 1 mm aluminum object without imparting damaging acceleration on the CubeSat. Consequently, CubeSats with masses of 12 kg, 16 kg, 24 kg, and 54 kg are all examined in the first set. A 1 N winding force is also utilized. The second set of simulations assumes a 2 mm debris object

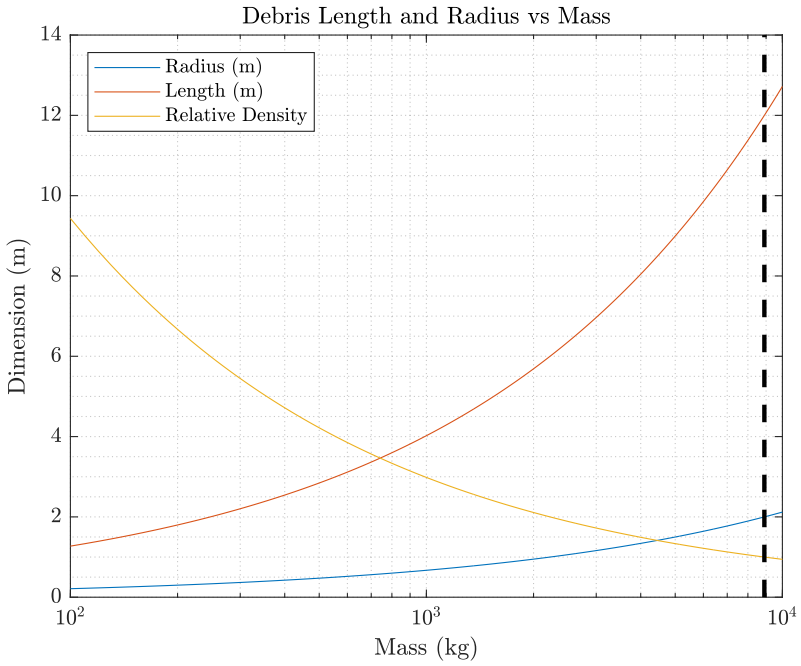

Fig. 12 Debris Object Dimensions vs Mass

Table 7 Harpoon Simulation Sets

Number	Object Thickness (m)	Firing Velocity (m/s)	Winding Force (N)	CubeSat Masses (kg)
1	0.001	15	1	12, 16, 24, 54
2	0.002	24	5	24, 54

thickness and a 24 m/s firing velocity, which immediately rules out the 12 kg and 16 kg CubeSat sizes as infeasible due to acceleration constraints. It also assumes a larger winding force of 5 N.

Figure 13 illustrates the probability of successful harpoon capture for various object and CubeSat sizes in the first set of simulations. Each of the data points shown on the plot was generated from analyzing the results of 25 randomized runs of TeRBoDOT. The most obvious trend in Figure 13 is the inverse correlation between debris object mass and success probability. It can be concluded that harpoon capture of small debris objects (with the corresponding decrease in capture distance) has a higher likelihood of success than capture of large objects (with a greater capture distance). Moreover, the relationship between success probability and object mass further suggests that changes in capture distance, and the resulting changes in precision, are greater drivers of feasibility than differences in debris object mass. For example, a $1,000$ kg object and a $10,000$ kg object are both multiple orders of magnitude larger than a 12 kg CubeSat, and both are minimally affected by any force it exerts. From a 12 kg CubeSat's perspective, the rotational behavior of the two objects is identical. Given the previously defined relationships between debris mass and tether length, the capture distance increases from 1.8 m for a $1,000$ kg object to 5.7 m for a $10,000$ kg object. In a similar way, position uncertainty increases from 0.2 m in each axis to 0.6 m. For a 12 kg CubeSat, the 44% difference in feasibility between the two objects suggests that one or both of these factors has a substantial impact on the outcome of the simulation. The same conclusion can drawn for the 16 kg and 24 kg CubeSats. The trend is not as clear for the 54 kg CubeSat, as the feasibility level drops off toward zero more quickly. The additional infeasibilities are almost all caused by constraint violations from collisions with the debris object. Instead of contacting the debris object at the harpoon penetration location with the tether completely wound in, the CubeSat strikes another location on the debris object's surface prior

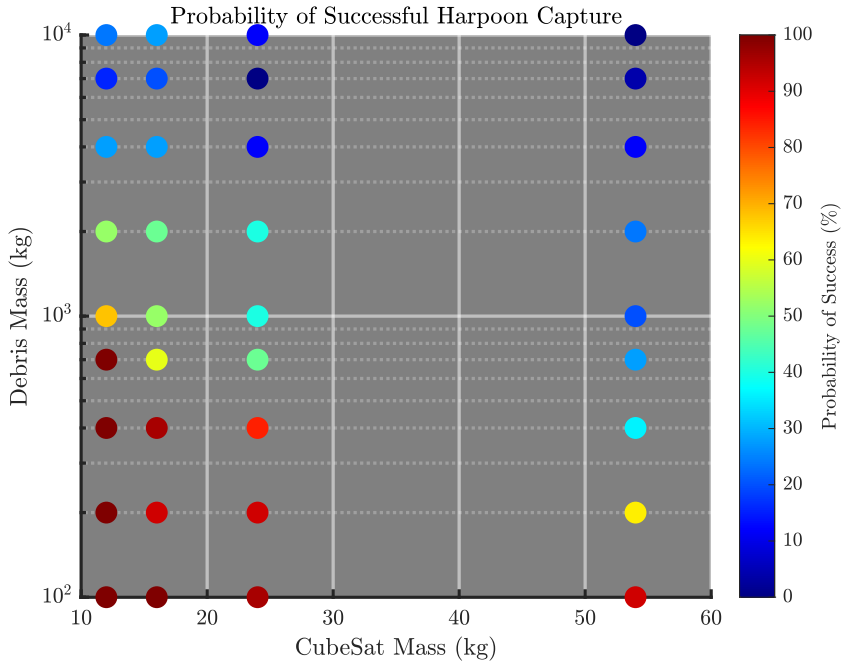

Fig. 13 Harpoon Feasibility Window with 1 *mm* Debris Object Thickness and 1 *N* Winding Force

to winding in the full tether length. This behavior suggests that the 1 *N* winding force may not be strong enough to maintain the 54 *kg* CubeSat on a stable approach path and prevent it from drifting away from the harpoon impact point during approach. As was the case for the 12 *kg*, 16 *kg*, and 24 *kg* CubeSats, a decrease in capture precision and increase in capture distance are also contributing factors for the additional collisions.

Figure 14 shows the results for the second set of harpoon simulations. The feasibility rates for the 24 *kg* and 54 *kg* CubeSats are markedly higher in this set of simulations than for the previous scenario. The 5 *N* winding force is more capable than the 1 *N* force of correcting any abnormalities in the satellite's position as it is pulled in, which results in fewer collisions and more successful approaches compared to the first scenario. Although the 54 *kg* CubeSat once again suffers from reduced feasibility at long distances, the probability of success remains above 32% for the largest debris object compared to 0% in the previous round of simulations. Two data points in Figure 14 require special attention. For the 24 *kg* CubeSat, the probability of success drops suddenly between the 4,000 *kg* object and the 7,000 *kg* object. The abruptness of this behavior is explained by a sudden increase in constraint violations due to excessive contact speed. A contact speed constraint violation is produced when a simulation has the appropriate position for docking, but is traveling at a velocity too great to accomplish the maneuver. For the 24 *kg* CubeSat, simulated capture of the 4,000 *kg* debris object generates no excessive velocity constraint violations. However, the 7,000 *kg* and 10,000 *kg* objects experience infeasibility from excessive contact speed in 28% and 40% of all the trials, respectively. In these cases, the 5 *N* winding force exerts too much of an acceleration on the CubeSat, causing it to contact the debris object at the appropriate angle and position but with too great a velocity for successful and controlled docking.

The two sets of simulations performed in this section suggest that harpoon-based capture is most likely to succeed when the object sidewall is thin enough to enable harpoon penetration ($1 - 2$ *mm* for aluminum), and a precise approach can be coordinated to a close-in firing point. Increased tether winding force leads to better control and higher success probabilities, as long as the CubeSat has sufficient inertia to avoid excessive contact speeds.

VII. Net Capture

In some cases, harpoon capture is not viable due to the thickness or structural integrity of the debris object. In these situations, net capture can represent an alternative capture technique that still retains the advantages of a tether-based

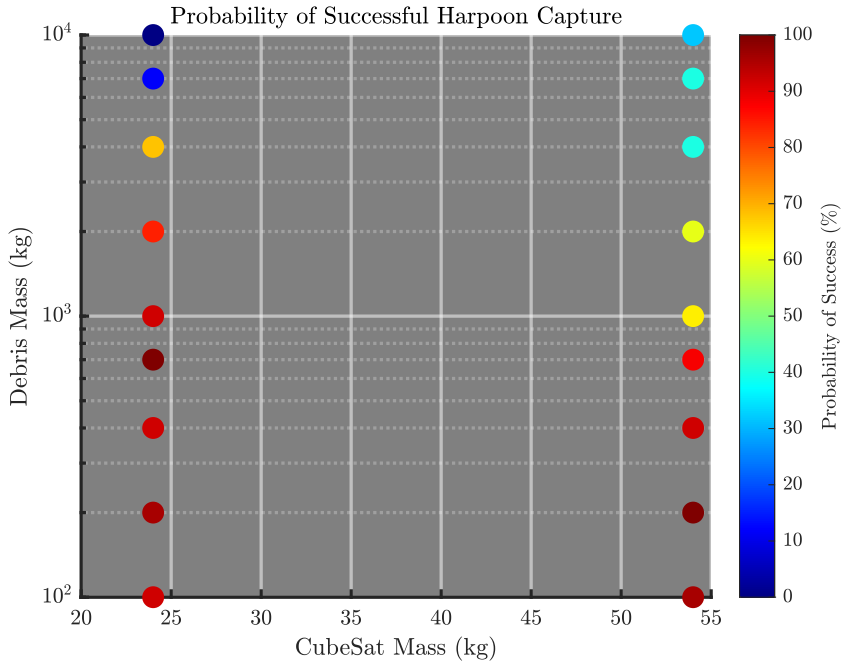

Fig. 14 Harpoon Feasibility Window with 2 *mm* Debris Object Thickness and 5 *N* Winding Force

method (further capture range and increased robustness to debris object angular momentum). The concept of operations for net-based capture is similar in many ways to that of harpoon-based capture. A point of attachment is established on the debris object from a distance, and the CubeSat and object are drawn together.

However, net deployment and dynamics add an additional layer of complexity. To achieve full-fidelity simulation of net-based capture scenarios, a realistic representation of the net itself is needed. Without such a model, it is impossible to precisely determine the net's interactions with the debris object's surface, predict the reaction forces the net exerts on the CubeSat, and determine the probability of a successful entanglement. Because development of such a model was outside the scope of this work, the deployment and entanglement phase of net capture is represented instead using the following assumptions:

1) The impact point of the net's center on the object's surface is predicted using pitch and yaw angles just as for the harpoon. This point is assumed to remain stationary with respect to the debris object throughout the entire simulation, and not shift in response to tension on the tether. If the debris object is rotating, the impact point is assumed to match the rate of rotation.
2) The flight time of the net is estimated by dividing the distance between the impact point and the CubeSat by the net's velocity relative to the debris object. The time required for the net to wrap around and entangle the debris object is estimated as 10 *s*, a value proposed by Botta [11] as the maximum time needed for a closure mechanism to close the net around the debris object.
3) The entire net deployment phase, encompassing firing, net flight, and entanglement, is propagated forward as a single time step. Because reaction forces on the CubeSat during deployment are not known, they are only calculated after the entanglement process is complete. When applied, the forces reflect the CubeSat's state at that moment. For example, if the tether pulls taut sometime during net deployment, the resulting spring force between the debris object and CubeSat is only detected and applied at the end of the time step.
4) Whenever the center of the net strikes the debris object, the net is assumed to successfully entangle the debris object. Cases where the net's center misses are treated as unsuccessful, since the simulation is not capable of determining what fraction of those cases would still allow the net to entangle and secure the debris object.

Given these assumptions, this chapter's discussion of net capture is not intended to represent all the nuanced dynamics involved in net entanglement, nor does it account for all the intricacies in the winding process caused by the

net's flexibility. Rather, it mirrors the harpoon capture analysis in focusing on the CubeSat's capabilities during the aiming, firing, and winding capture phases. Comparisons are then drawn between net and harpoon methods regarding these capabilities. Despite the limitations on net fidelity, differences observed between the net and harpoon capture methods can still provide insight into the effects of changing capture distance, payload deployment velocity, and winding delay time for tether-based capture methods in general.

A. Aim and Incidence Angle

As with harpoon capture, three case studies are conducted to assess the performance of a net-based capture method in successfully targeting debris of different sizes. In this context, a "successful" targeting event is defined in a similar way to the harpoon capture scenario. To be successful, the trajectory of the net's center must lead directly to an impact with the debris object's surface. Because of the large surface area of the net, scenarios in which the net's center "misses" may still be successful if the error in aim is small enough to permit one side of the net to envelop and entangle the debris object. However, analysis of those scenarios falls outside the scope of this work.

The net capture case studies examine the same three debris objects examined for harpoon capture: the SL-16 rocket body, SL-8 rocket body, and a small cylindrical debris object 1 m long and 0.5 m in diameter. Capture distance is set equal to 20 m, representative of the net capture CONOPS, and the position box is 4 $m \times 4$ $m \times 4$ m. Note that both values are larger for net capture than for the harpoon case studies, representing the further capture distance required to ensure full net deployment.

Results are shown in Figure 15, and indicate the net's center has a 99.02% chance of striking the SL-16 rocket body. The probability reduces to 82.68% for the SL-8 and 14.58% for the small cylindrical debris object. Due to the further (20 m) capture distance, the net targeting probabilities are significantly lower than for the harpoon capture cases, where all three objects had an 84-100% probability of impact at a 5 m range. As mentioned previously, the probability of successful capture could be much higher if certain kinds of off-nominal net impacts still result in success. Particularly if the net used is much wider than the debris object, the net's center does not necessarily have to strike the object to enable entanglement. Future work on net-based debris capture is needed to determine the robustness of the method for capture scenarios in which the net strikes the debris object off-center. Because the concept of incidence angle has little meaning for a net that is intended to wrap around the debris object regardless of angle, a color bar is not included in Figure 15. Instead, the permissible yaw and pitch stabilities are shown for all trials in which the net's center struck the debris object.

B. Net Parameters and Deployment

The net used for capture is inspired by Botta's work on net deployment for space debris capture [11] [12]. In her debris capture case studies, Botta assumes square nets with a side length roughly twice as long as the debris object. Masses at each corner of the net are provided an initial velocity of 2.5 m/s at an angle roughly 35° outwards from the intended direction of net travel. The corner masses, in turn, accelerate and spread the net in flight. While the mesh size can vary considerably, it is assumed in this work that the mesh width is 5% of the net's side length. In other words, a 10×10 m^2 net has a square mesh size of 0.5 m. This design choice means that the net mass is approximated as:

$$m_{net} = 2l_{side}(N+1)\rho_{net} \tag{31}$$

Where N is the ratio of side length to mesh size ($N = 20$ in this case), l_{side} is the length of one side of the net, and ρ_{net} is the mass per unit length of the net material. Botta assumes a value of $547 * 10^{-6}$ kg/m for ρ_{net}, which is applied here too. By combining and simplifying these values, the net mass can be expressed as:

$$m_{net} = (45.948 * 10^{-3})l_{deb} \tag{32}$$

Botta further suggests that the masses installed at the corners of the net should have a combined mass between 70-230% of the net's mass [11]. To keep system mass low, a value on the lower end of the allowable spectrum—100%—is assumed in this work, meaning that the sum of the corner masses is also equal to the net's mass.

The optimal firing range is approximated by determining the point in time when the net reaches full expansion, assuming the corner masses travel in straight lines along the directions they are fired. If the net has a side length of l_{side}, and each of the four corner masses is fired diagonally at an angle of $\theta_f = 35°$ outward from the direction of net motion, the distance to full expansion is equal to:

$$d_{firing} = \frac{l_{side}\sqrt{2}/2}{tan(\theta_f)} = 1.0099 * l_{side} \tag{33}$$

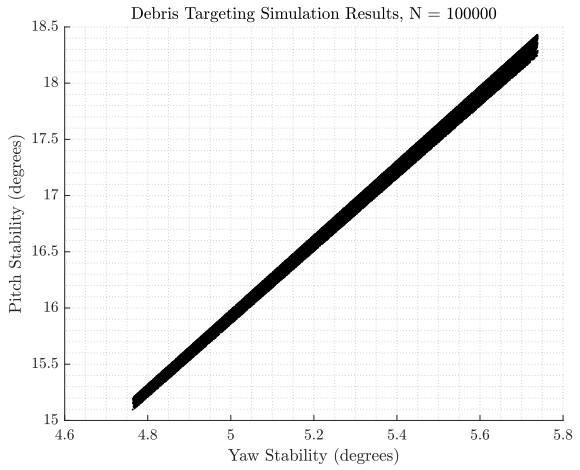

(a) SL-16 Rocket Body

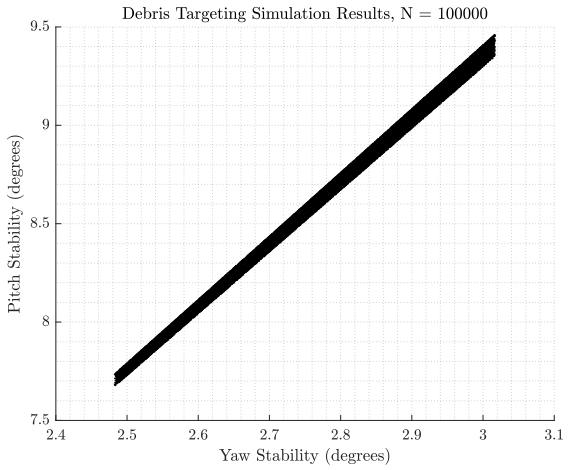

(b) SL-8 Rocket Body

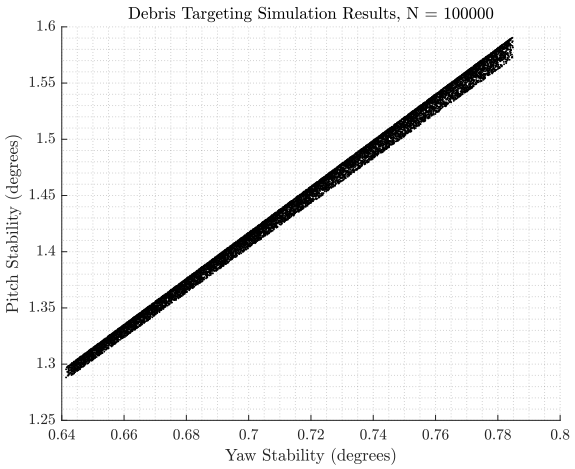

(c) Small Cylindrical Debris

Fig. 15 Net Targeting Simulations, 20 m Distance

As with the harpoon capture scenario, it is necessary to consider the conditions in which acceleration from net firing causes damage to the CubeSat. Recoil forces are exerted on the CubeSat from the deployment of the net's four corner masses, each from its own respective tube. The firing tubes are assumed to have a length of $l_{tube} = 0.15\ m$. During firing, the corner masses each experience an acceleration equal to:

$$a_{firing} = \frac{v_{firing}^2}{2l_{tube}} \tag{34}$$

The CubeSat's acceleration is expressed in terms of a_{firing}. To avoid structural damage, the CubeSat's recoil acceleration at the moment of net firing is limited to 1 G, producing the following constraint:

$$\frac{m_{CM}}{m_{sat}} a_{firing} cos(\theta_f) \leq 1G \tag{35}$$

Where m_{CM} is the combined mass of the net's corner masses and m_{sat} is the total mass of the CubeSat. A feasibility window is constructed to show the recoil acceleration experienced for 12 kg, 16 kg, 24 kg, and 54 kg CubeSats. The

quantities on the left side of the constraint equation shown above are all assumed constant except for m_{sat} and m_{CM}; the second quantity in turn is a function of m_{deb} because of the relationship between m_{CM} and m_{net}.

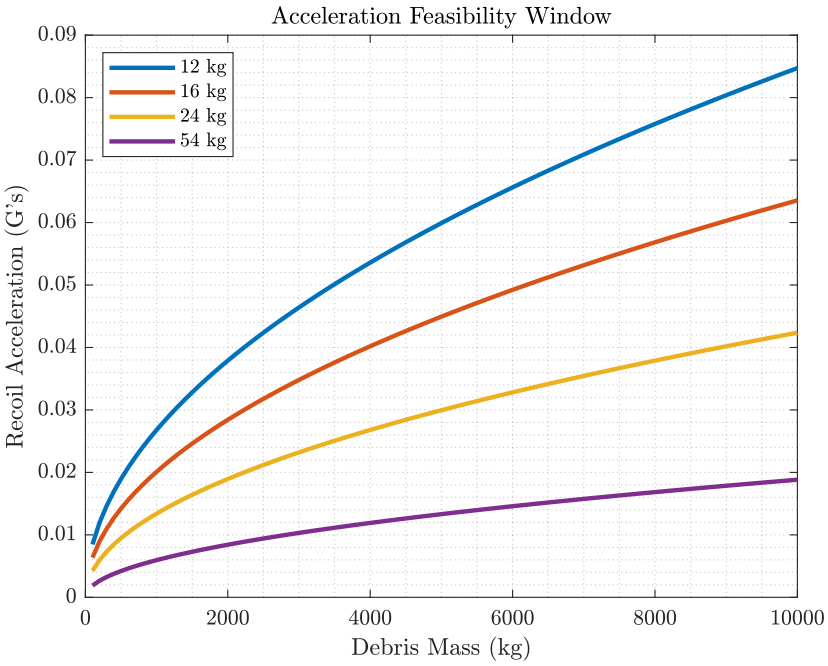

Fig. 16 Net Capture Acceleration Feasibility Windows

The feasibility window is shown in Figure 16 and illustrates net firing acceleration as a function of m_{deb}, with separate lines for 12 kg, 16 kg, 24 kg, and 54 kg satellites. Since the upper safe bound on acceleration is assumed to be 1 G, it is clear from the figure that the net firing parameters selected above are unlikely to result in damage to the CubeSat during firing. Even for the smallest CubeSat examined, the net never induces an acceleration more than 10% of the upper bound.

C. Winding and Docking

A round of Monte Carlo simulations is performed for the net capture scenario in the same way as for harpoon capture. In this case, Equation 33 is used to relate capture distance to object size. Tether length is assumed to be 50% longer than d_{firing}, in order to reduce the likelihood of the CubeSat drifting out of tether range before the net closes. Given a debris object mass range of $100 - 10,000\ kg$, capture distance varies between $2.6 - 25.7\ m$ and tether length varies between $3.9 - 38.5\ m$. Each data point in the net feasibility windows is constructed using 25 randomized TeRBoDOT simulations. The CubeSat is assumed to be located at a distance of $d_{firing} + r_{deb}$ along the X-axis at the moment of net firing (as measured from the debris object's center of mass), with a precision equal to $\pm 0.1 * d_{firing}$ in each axis. Since this capture distance is further than for the harpoon case, a 2 N winding force is used initially instead of 1 N to expedite capture and allow for greater control of the CubeSat's movement during winding.

The feasibility window is illustrated in Figure 17. Simulation results suggest that the net capture scenario examined here has lower feasibility than its harpoon counterpart, a logical outcome given that the net scenario requires a further initial separation. Most of the constraint violations are due to collisions with the debris object that occur when the CubeSat is unable to wind itself in to the tether attachment point at the net's center. Variations in feasibility correlate with debris object mass, suggesting a tradeoff between starting distance and success probability. The results of this set of simulations indicate that net capture is most likely to succeed at closer ranges, corresponding to smaller debris objects that can be captured in smaller nets.

Success of the 12 kg and 16 kg CubeSats is hindered by excessive contact velocity when attempting to capture debris objects larger than 200 kg and 700 kg, respectively. In such cases, the CubeSat's approach direction satisfies

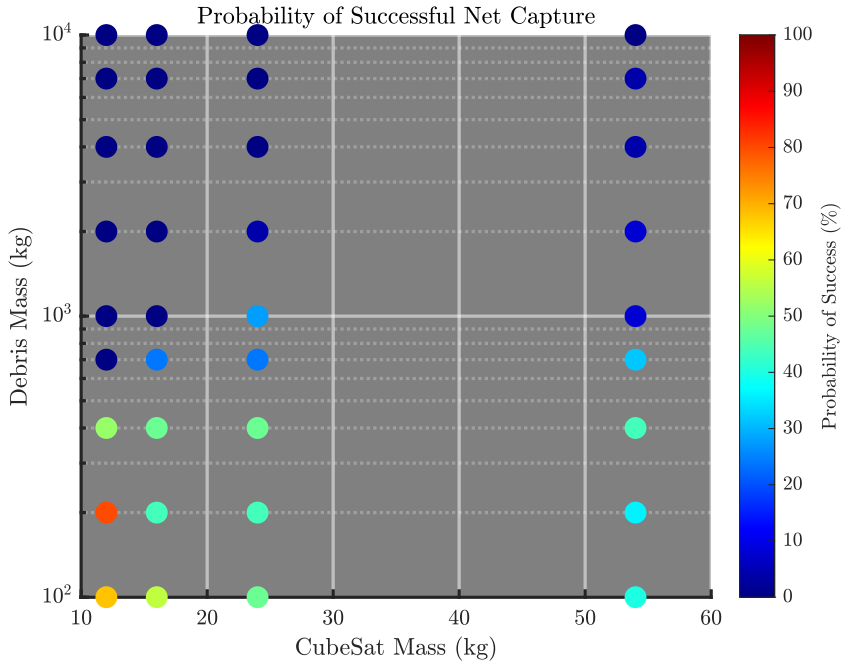

Fig. 17 Net Feasibility Window with 5 *mm* Debris Object Thickness and 2 *N* Winding Force

constraints, but the relative velocity between the CubeSat and debris object is too high for a successful capture. For $2,000\ kg$ objects, 16-20% of the 12 kg and 16 kg CubeSat trials are rendered infeasible due to excessive velocity. Another set of simulations is performed with a 1 N force in an attempt to increase feasibility across the smaller CubeSat sizes. All other parameters are the same as for the first set of net simulations.

The second set of net simulations is shown in Figure 18. Using a 1 N winding force decreases the amount of infeasibilities resulting from excessive contact speed, but it has mixed effectiveness in improving the overall feasibility of the net capture scenario. In all but three cases, the lower force actually reduces feasibility for debris objects smaller than $1,000\ kg$ across all CubeSat sizes. In six of the eight cases between $1,000 - 2,000\ kg$, the lower force increases the overall feasibility value by as much as 16%. A detailed comparison of feasibility vs winding force for various CubeSat sizes is beyond the scope of this work, but the results obtained in both harpoon and net capture simulations indicate even small changes in winding force have an influence on success probability.

VIII. Summary and Conclusions

In this work, robotic arms, harpoons, and nets are examined as possible methods of debris object capture for CubeSat ADR missions. The robotic arm is found to be suitable for debris objects that possess negligible angular velocity and accessible gripping points. The harpoon and net methods demonstrate an ability to secure slow-rotating objects with angular velocities of $1.4°/s$. Within the simulation environments utilized, harpoon capture has a success probability higher than 80% for two-thirds of the capture scenarios involving debris object masses up to $1,000\ kg$. Due to the relationship between debris dimensions and capture distance, this subset corresponds to an initial separation between the object and CubeSat of 1.8 m or less. The net capture scenarios exhibit lower feasibility values than the harpoon scenarios due to longer starting distances, but success probabilities above 50% are determined for nearly one-third of the scenarios with debris object masses 200 kg or below (starting distance less than 3.6 m). Positioning uncertainty is understood to decrease with separation distance, meaning that in a majority of the test scenarios, the harpoon method assumes a higher degree of position knowledge and control compared with the net. Furthermore, simulation of the net capture method requires major assumptions about the net deployment process given the lack of a high-fidelity net model. Future work should explore in more detail the relationship between distance and feasibility for both harpoon and net

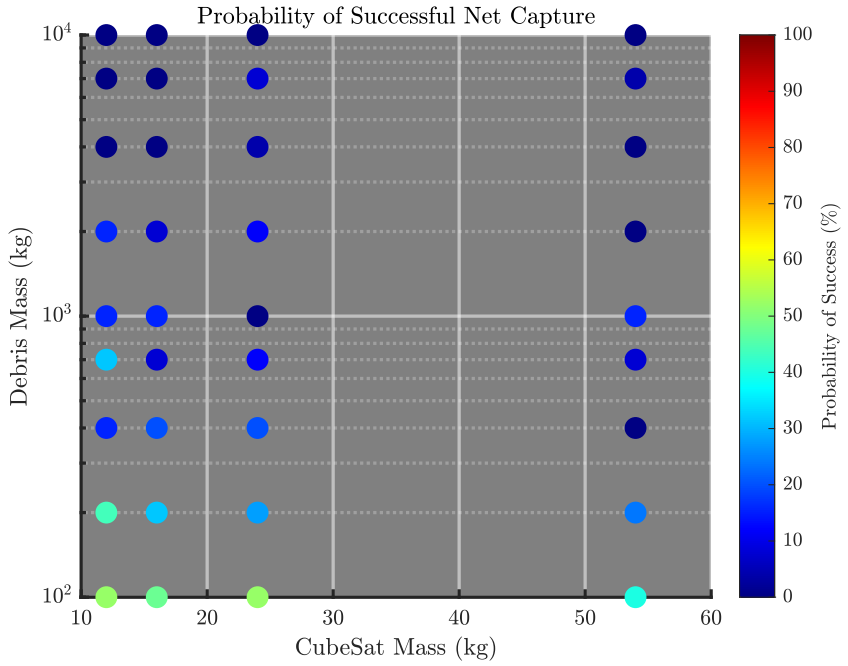

Fig. 18 Net Feasibility Window with 5 *mm* Debris Object Thickness and 1 *N* Winding Force

capture scenarios, as well as the correlation between winding tension and feasibility.

Acknowledgments

One of the authors, Chris Clark, was supported by a Draper Laboratory Fellowship. The authors would like to acknowledge useful discussions and insight from the students in the Space Systems Lab at MIT.

References

[1] Hakima, H., and Emami, M. R., "Concurrent attitude and orbit control for Deorbiter CubeSats," *Aerospace Science and Technology*, Vol. 97, 2020, p. 105616. https://doi.org/10.1016/j.ast.2019.105616. URL http://www.sciencedirect.com/science/article/pii/S1270963819321030.

[2] McCormick, R., Austin, A., Wehage, K., Backus, S., Miller, R., Leith, J., Bradley, B., Durham, P., and Mukherjee, R., "REMORA CubeSat for large debris rendezvous, attachment, tracking, and collision avoidance," *Proceedings of the 2018 IEEE Aerospace Conference*, Big Sky, MT, 2018. https://doi.org/10.1109/AERO.2018.8396814.

[3] Hakima, H., Bazzocchi, M. C. F., and Emami, M. R., "A deorbiter CubeSat for active orbital debris removal," *Advances in Space Research*, Vol. 61, No. 9, 2018, pp. 2377–2392. https://doi.org/10.1016/j.asr.2018.02.021, URL http://www.sciencedirect.com/science/article/pii/S0273117718301613.

[4] Clark, J. R., "Space-based laser guide stars for astronomical observatories," Thesis, Massachusetts Institute of Technology, 2020. URL https://dspace.mit.edu/handle/1721.1/129146 accepted: 2021-01-06T18:31:22Z ISBN: 9781227276690.

[5] Guo, J., and Han, C., "Where is the Limit: The Analysis of CubeSat ADCS Performance," *Proceedings of the Small Satellites, System & Services Symposium*, Valletta, Malta, 2016.

[6] Liou, J. C., "Orbital Debris Quarterly News," *Orbital Debris Quarterly News*, Vol. 15, No. 2, 2011, pp. 4–6. URL https://orbitaldebris.jsc.nasa.gov/quarterly-news/pdfs/odqnv15i2.pdf. published by the NASA Orbital Debris Program Office.

[7] Forshaw, J. L., Aglietti, G. S., Fellowes, S., Salmon, T., Retat, I., Hall, A., Chabot, T., Pisseloup, A., Tye, D., Bernal, C., Chaumette, F., Pollini, A., and Steyn, W. H., "The active space debris removal mission RemoveDebris. Part 1: From

concept to launch," *Acta Astronautica*, Vol. 168, 2020, pp. 293–309. https://doi.org/10.1016/j.actaastro.2019.09.002, URL http://www.sciencedirect.com/science/article/pii/S0094576519312512.

[8] Aglietti, G. S., Taylor, B., Fellowes, S., Salmon, T., Retat, I., Hall, A., Chabot, T., Pisseloup, A., Cox, C., Zarkesh, A., Mafficini, A., Vinkoff, N., Bashford, K., Bernal, C., Chaumette, F., Pollini, A., and Steyn, W. H., "The active space debris removal mission RemoveDebris. Part 2: In orbit operations," *Acta Astronautica*, Vol. 168, 2020, pp. 310–322. https://doi.org/10.1016/j.actaastro.2019.09.001, URL http://www.sciencedirect.com/science/article/pii/S0094576519312500.

[9] Banik, J., "Structural Scaling Metrics For Tensioned-Blanket Space Systems," PhD, The University of New Mexico, Jul. 2014. URL https://digitalrepository.unm.edu/ce_etds/15.

[10] Wagner, W. A., and Keller, R. B., "Liquid Rocket Metal Tanks and Tank Components," Technical Report NASA-SP-8088, NASA Lewis Research Center, Cleveland, OH, May 1974. URL https://ntrs.nasa.gov/api/citations/19750004950/downloads/19750004950.pdf.

[11] Botta, E. M., "Deployment and Capture Dynamics of Tether-Nets for Active Space Debris Removal," PhD, McGill University, Montreal, Canada, Nov. 2017.

[12] Botta, E. M., Miles, C., and Sharf, I., "Simulation and tension control of a tether-actuated closing mechanism for net-based capture of space debris," *Acta Astronautica*, Vol. 174, 2020, pp. 347–358. https://doi.org/10.1016/j.actaastro.2020.04.052, URL https://www.sciencedirect.com/science/article/pii/S009457652030268X.